Critical roles of edge turbulent transport in the formation of high-field-side high-density front and density limit disruption in J-TEXT tokamak

Original
Critical roles of edge turbulent transport in the formation of high-field-side high-density front and density limit disruption in J-TEXT tokamak / Shi, Peng; Wang, Yuhan; Gao, Li; Sun, Hongjuan; Yang, Qinghu; Xu, Xin; Shen, Chengshuo; Chen, Yanqiu; Tao, Qinlin; Chen, Zhipeng; Wu, Haosheng; Wang, Lu; Chen, Zhongyong; Wang, Nengchao; Yang, Zhoujun; Li, Jingchun; Ding, Yongohua; Pan, Yuan. - In: NUCLEAR FUSION. - ISSN 0029-5515. - (2025). [10.1088/1741-4326/ae0951]

Publisher:
IOP

Published
DOI:10.1088/1741-4326/ae0951

IAEA nuclear fusion

PAPER • OPEN ACCESS

Critical roles of edge turbulent transport in the formation of high-field-side high-density front and density limit disruption in J-TEXT tokamak

To cite this article: Peng Shi *et al* 2025 *Nucl. Fusion* **65** 116005

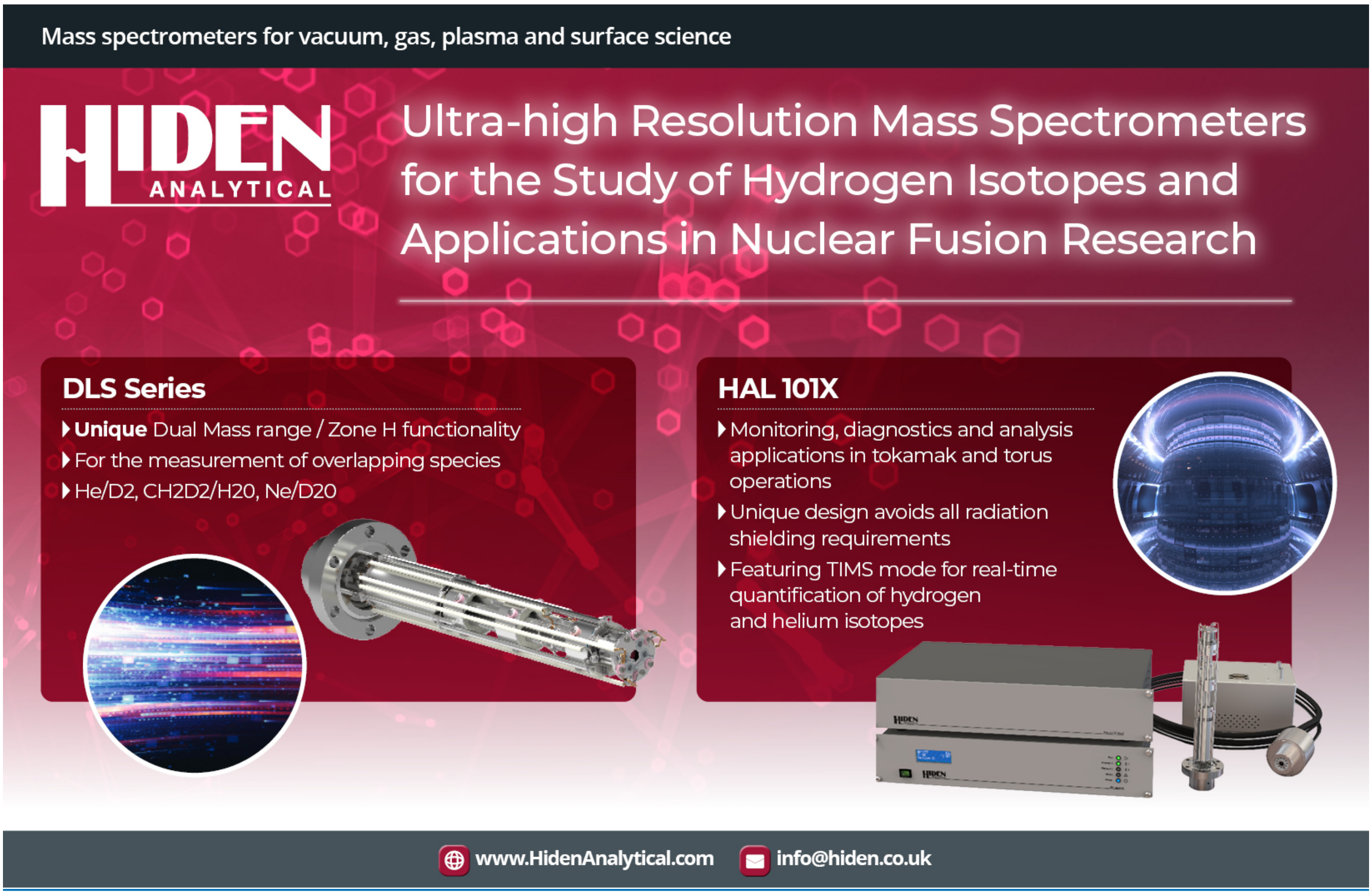

OPEN ACCESS
IOP Publishing | International Atomic Energy Agency

Nuclear Fusion

Nucl. Fusion **65** (2025) 116005 (11pp)

https://doi.org/10.1088/1741-4326/ae0951

Critical roles of edge turbulent transport in the formation of high-field-side high-density front and density limit disruption in J-TEXT tokamak

Peng Shi[1,2,3], Yuhan Wang[2], Li Gao[2,*], Hongjuan Sun[3], Qinghu Yang[2], Xin Xu[2], Chengshuo Shen[2], Yanqiu Chen[2], Qinlin Tao[2], Zhipeng Chen[2], Haosheng Wu[4], Lu Wang[2], Zhongyong Chen[2], Nengchao Wang[2], Zhoujun Yang[2], Jingchun Li[5], Yongohua Ding[2], Yuan Pan[2] and J-TEXT Team[a]

[1] Institute of Plasma Physics, Chinese Academy of Sciences, Hefei 230031, China
[2] International Joint Research Laboratory of Magnetic Confinement Fusion and Plasma Physics, State Key Laboratory of Advanced Electromagnetic Engineering and Technology, School of Electrical and Electronic Engineering, Huazhong University of Science and Technology, Wuhan 430074, China
[3] United Kingdom Atomic Energy Authority, Culham Centre for Fusion Energy, Culham Science Centre, Abingdon, Oxon OX14 3DB, United Kingdom of Great Britain and Northern Ireland
[4] NEMO Group, Dipartmento Energia, Politecnico di Torino, Corso Duca degli Abruzzi 24, 10129 Torino, Italy
[5] Shenzhen Key Laboratory of Nuclear and Radiation Safety, College of Physics and Optoelectronic Engineering, Shenzhen University, Shenzhen 518060, China

E-mail: gaoli@mail.hust.edu.cn

Received 5 August 2023, revised 16 September 2025
Accepted for publication 19 September 2025
Published 6 October 2025

Abstract

This article presents an in-depth study of the sequence of events leading to density limit disruption in J-TEXT tokamak plasmas, with an emphasis on boundary turbulent transport and the high-field-side high-density (HFSHD) front. These phenomena have been extensively investigated using a Langmuir probe and Polarimeter–interferometer diagnostics. The research reveals a consistent pattern of events as the plasma density ramps up: the collapse of the sheared radial electric field, the enhancement of the boundary quasi-coherent turbulence ($50 \sim 80\,\mathrm{kHz}$), the increase in boundary particle transport induced by this turbulence, edge cooling and the emergence of the HFSHD front. These phenomena occur once the plasma density exceeds a critical value. Importantly, by exploring plasmas with varying edge safety factor (q_a), it is revealed that the density thresholds for these phenomena are all inversely proportional to q_a. The findings offer valuable insights into the mechanisms underlying density limit disruptions in tokamak plasmas, suggesting that the enhancement of edge turbulent transport plays a crucial role in the edge cooling and triggering the HFSHD front. For the first time, a strong link

---

[a] See Ding *et al* 2024 https://doi.org/10.1088/1741-4326/ad336e for J-TEXT Team.
[*] Author to whom any correspondence should be addressed.

between the edge turbulent transport and the HFSHD front has been observed. In addition, the evolution of the boundary electron temperature across various q_a plasmas can further validate the link between the edge turbulent transport and the HFSHD formation.

Keywords: high-field-side high-density, density limit disruption, turbulence and transport, MARFE

(Some figures may appear in colour only in the online journal)

1. Introduction

High density is a prerequisite for the operation of future fusion reactors since the power produced by fusion is proportional to the square of plasma density. To achieve higher economic efficiency in future large tokamaks, a high plasma density is highly desirable for the next-step tokamaks, such as the International Thermonuclear Experimental Reactor (ITER) and Chinese Fusion Engineering Testing Reactor [1, 2]. However, experiments in tokamaks show that the plasma operating densities always have an upper limit. At present, the Greenwald density (line-averaged) scaling $n_G\left[10^{20}\mathrm{m}^{-3}\right] = I_P\left[\mathrm{MA}\right]/\pi a^2\left[\mathrm{m}^2\right]$ is empirical for the density limit, which was found to be widely applicable to devices such as the Alcator, DIII and PBX [3, 4].

Experimental and theoretical studies of the density limit have been pursued for decades, leading to a multitude of explanations for the underlying physical mechanisms. In experiments where the plasma density is increased via continuous gas puffing, various instabilities have been observed as the plasma density gradually ramps up to the density limit disruption. Results across different devices have revealed common characteristics of these physical phenomena during the process of density limit disruption [5, 6]. For instance, thermal-radiation instabilities [7, 8], edge cooling [9], boundary constraint deterioration and eventual MHD instabilities [4, 10] are consistently observed during the process of density ramp-up. Foundational theoretical work by Stacey has demonstrated that these diverse outcomes can often be understood as manifestations of different types of thermal instabilities—such as core MARFEs, confinement degradation, or global radiative collapse—which are selectively triggered depending on the specific operational conditions [11]. The highly reproducible nature of these phenomena and their occurrence at the plasma boundary suggest that the boundary plasma behavior plays an important role in the physical mechanism of density limited disruption [12]. Moreover, it was found that the Greenwald density limit could be exceeded by optimizing fueling techniques, which can increase the central plasma density while maintaining the boundary plasma density. Classic experiments on DIII-D, for example, successfully utilized pellet injection to create peaked density profiles that significantly surpassed the Greenwald limit, thereby establishing that the local edge or separatrix density, rather than the line-averaged value, is the more fundamental limiting parameter [13, 14]. This discovery provides strong evidence that the evolution of the boundary parameters plays a crucial role in determining the density limit.

In experimental researches on the density limit disruption in tokamaks, two factors were found to play key roles in limiting the achievable plasma density: thermal instability and turbulent transport. The thermal instability is mainly exemplified by MARFE [15], one of the most remarkable macro-phenomena observed in the process of density limit disruption. MARFE is characterized by high electron density, low temperature, strong volumetric recombination, and commonly occurs at the high field side (HFS) near the inner wall of the tokamak in limiter [16]. Over decades, MARFEs have been observed on various tokamaks, such as TFTR [17], TEXTOR [18], JT-60 [19], HT-7 [20], FTU [21] and so on. In divertor plasmas, the phenomena tend to manifest close to the X-point region, and are often accompanied by divertor detachment, which is referred to as a 'X-point MARFE' or 'divertor MARFE' [22–24].

Recently, a high-field-side high-density (HFSHD) phenomenon, which is a poloidally localized high-density region in the HFS scrape-off layer (SOL), was reported by Potzel [25]. In ASDEX-U and JET divertor plasmas, the HFSHD front appears near the inner target and moves to the X-point as the plasma density increases, followed by the X-point MARFE and divertor detachment [26–28]. The HFSHD shares many similarities to MARFE, such as both occurring at the HFS boundaries, exhibiting localized high density and related to the detachment. However, there are also subtle differences between the two phenomena. The radiation power from the region of the HFSHD front is significantly lower than MARFE. The HFSHD front is more stable at the inner target or HFS edge across a broad range of plasma densities, which is in contrast to the unstable behavior of MARFE [29, 30]. It is challenging to entirely distinguish between MARFE and HFSHD based on phenomenology. However, in terms of terminology, the term of 'MARFE' emphasizes the localized strong radiation power, while the 'HFSHD' puts more emphasis on localized high density. A similar phenomenon, MARFE or HFSHD, was also often observed in J-TEXT high-density plasmas. We called it MARFE in our first publication [31], and changed it to HFSHD in a recent article [32]. The reason is that the local high density at the HFS edge is much more remarkable than the radiation power on J-TEXT, as illustrated by figure 3 in [32]. In fact, J-TEXT is a rare limiter device, without strong radiation power observed at the inner edge after the appearance of MARFE or HFSHD. This might be attributed to the unique limiter configuration of J-TEXT. Unlike most devices using toroidal limiters at the HFS, J-TEXT utilizes poloidal limiters with small area. Thus, it is anticipated that there is less impurity accumulation at the HFS edge on J-TEXT than other devices. Based on this observation, the author speculates that the MARFE is a result of a HFSHD front with local impurity accumulation.

In addition to thermal-radiation instabilities, micro-turbulence instability is also found to play an important role in boundary cooling and density limit disruption. In the early years, an enhanced micro-turbulence and particle transport was observed in TEXT [33] and Alcator C-Mod [34] high-density plasmas. The theory by D'lppolite has proven that turbulent transport can drive the density limit in plasma without impurities [35]. In recent years, a collapse of edge flow shear and a decrease in the ratio of Reynolds power to turbulence production during the ramp-up of plasma density have been measured on both HL-2A [36] and J-TEXT [37]. These findings are consistent with the theoretical prediction by Hajjar and Diamond [38]. Furthermore, by applying an electrode biasing at the plasma edge to increase the edge flow shear, the plasma confinement was found to be improved [39] and the maximum operating density can be increased [40]. This can further confirm the role of edge turbulent transport in the density limit in tokamaks.

As discussed above, there are numerous publications addressing thermal instability or turbulent transport in high-density plasmas. However, there are few articles studying the link between thermal instability and turbulence. In theory and simulation, Tokar suggested that the anomalous transport induced by the drift resistive ballooning instability could increase nonlinearly in the high-density regime and lead to a surge of impurity radiation at the plasma edge [41]. In recent J-TEXT experiments, the appearance of 'MARFE or HFSHD' and enhancement of turbulent transport are observed simultaneously. The sequence of their occurrence and the relationship between their critical densities and the edge safety factor q_a have been carefully investigated in the present article. The results indicate that the increase in turbulent transport at the edge is responsible for the edge cooling and the occurrence of 'MARFE or HFSHD'. This may be the first experimental evidence revealing the link between micro-turbulence and macro-thermal instability.

The rest of the paper is organized as follows: section 2 describes the experimental setup and main diagnostics for the investigation of the edge turbulence behavior and HFSHD front in the J-TEXT tokamak. Section 3 presents the experimental results during the density ramp-up. Section 4 presents conclusion and discussion.

2. Experimental setup

The J-TEXT tokamak (formerly TEXT-U [42]) is a conventional medium-sized tokamak with a major radius of $R_0 = 1.05$ m and minor radius of $a = 0.25 \sim 0.29$ m. The first wall and the limiter are covered with carbon tiles. In this experiment, we utilized three different positions of limiters—top, bottom and outer (figure 1(*a*)), all located at $r_{\text{Limiter}} = 25.5$ cm. It is noteworthy that there is no limiter at the HFS in our experiments (it was removed recently for the HFS divertor operation) [43], which is quite different to the experiments in our previous publication [31, 32]. The arrangement of the main diagnostics is shown in figure 1. The line-integrated electron density is measured by a multi-channel far-infrared laser polarimeter–interferometer system (POLARIS) [44]. This system views the plasma vertically at intervals of 3 cm in the radial mid-plane, ranging from $r = -24$ cm to $r = +24$ cm, thereby covering the main plasma region ($|r| < 0.94a$), where $r = R - R_0$, as shown in figures 1(*a*) and (*b*). Here, $r < 0$ and $r > 0$ correspond to the HFS and the low field side (LFS), respectively.

A 36-channel photo-diode array (PDA) system is used to measure the line emission of hydrogen α (H_α) [45]. This system, similar to POLARIS, also covers the HFS and LFS of the tokamak. The sight line of the inner-most three chords go through the area where the'MARFE or HFSHD' are located, and only the channels employed in this experiment are shown in figure 1(*a*). The electrostatic probe arrays, also known as the combined Langmuir probe (CLP) [46], are mounted on the window Port#13 at the device's top (figure 1(*b*)). The configuration of the Langmuir probe array is shown in figure 1(*c*). The CLP consists of eight graphite probes, each with a diameter of 2 mm. Probes 1–4 are situated on step 1 with a length of 3 mm, while probes 5–8 are on step 2 with the same length. The connecting line of pins 5 and 7 align with the direction of the ring, avoiding the shadow effect between the probes. Pins 1 and 3 are distributed along the toroidal direction as a pair of Mach probes. Pins 2 and 4 measure the average floating potential on step1 $V_{f,\text{step1}} = (V_{f,2} + V_{f,4})/2$. Pins 6 and 8 spacing $d = 7$ mm are used to measure the average floating potential on step2 $V_{f,\text{step2}} = (V_{f,6} + V_{f,8})/2$. Pins 5 and 7 are biased to form a double probe to acquire the ion saturation current $I_s = (V_{+,5} - V_{-,7})/R_{\text{shunt}}$, where R_{shunt} refers to the sample resistor in the double probe circuit. Based on the above configuration, the electron temperature T_e, electron density n_e, the poloidal electric field E_p and the radial electric field E_r can be measured simultaneously by CLP. Electron temperature is inferred by $T_e = (V_{+,5} - V_{f,\text{step2}})/\ln 2$. Electron density is inferred by $n_e = I_s/(0.49eA_{\text{eff}}C_s)$, where e is the elementary charge, $C_s = \sqrt{k_B(ZT_e + T_i)/m_i} \approx \sqrt{2k_BT_e/m_i}$ is ion sound speed and A_{eff} is the effective current collection area. Plasma potential is inferred by $\varphi_p = V_{f,\text{step2}} + 2.5T_e$, and then the radial electric field is inferred from $E_r = -\nabla_r\varphi_p \approx -\nabla_r V_{f,\text{step}} - 2.5\nabla_r T_e/e$. The poloidal electric field is computed as $E_p \approx (V_{f,6} - V_{f,8})/d$, here, d is the spacing between pins 6 and 8.

Experimental investigations were undertaken on the J-TEXT tokamak utilizing a limiter configuration in ohmic hydrogen discharges. Continuous gas puffing was applied throughout the experiments. The ensuing experimental results are based on two distinct discharge conditions, with the corresponding parameters described as follows, unless specially stated otherwise:

[I] A set of shots with density ramp-up in single shot: plasma current $I_P = 120$ kA, toroidal magnetic field $B_t = 1.7/1.9/2/2.2\ T$, safety factor $q_a = 4.4/4.9/5/5.5$ at the plasma edge, with the central line-averaged electron density ramping up in the range $2 \sim 4.5 \times 10^{19}\text{m}^{-3}$, and the

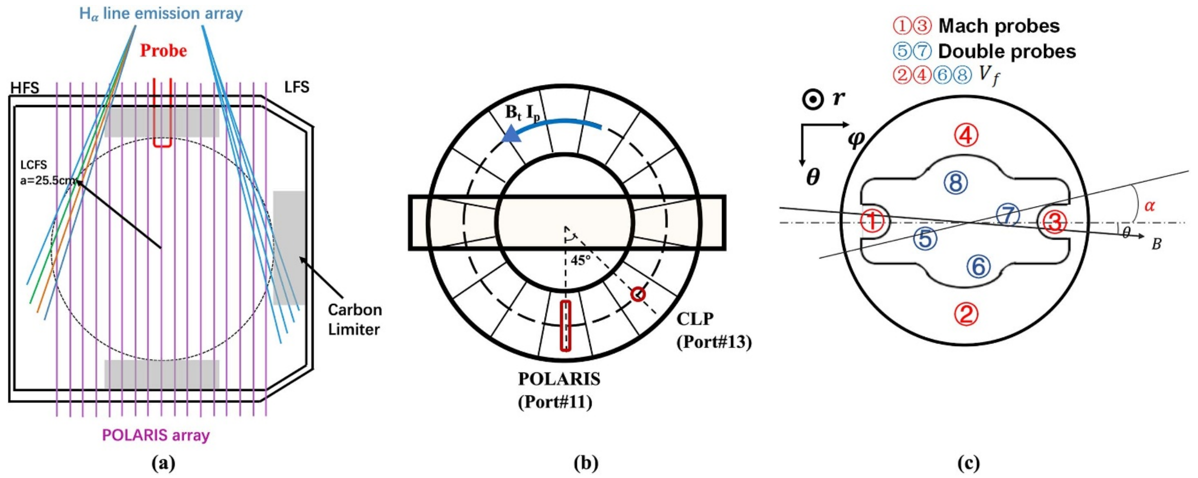

Figure 1. Arrangement of the main diagnosis. (*a*) Cross-section of J-TEXT tokamak, viewing lines of the J-TEXT PDA (in blue) and POLARIS (in magenta), respectively. (*b*) Top view of J-TEXT tokamak, POLARIS and CLP are toroidally separated by 45°. (*c*) The configuration of CLP array.

Greenwald density limit as $n_G = 5.87 \times 10^{19}\mathrm{m}^{-3}$. The CLP remains fixed at $r = 23\,\mathrm{cm}$ in these shots, and a typical plasma trace is shown in figure 2.

[II] A set of shots with lifting densities shot by shot and constant density in each shot: plasma current $I_P = 120\,\mathrm{kA}$, toroidal magnetic field $B_t = 1.7/1.9/2$, safety factor $q_a = 4.4/4.9/5$. The central line-averaged electron density hovers around 1.5–$3\times10^{19}\mathrm{m}^{-3}$. The CLP reciprocates to $r = 23\,\mathrm{cm}$ in each shot, providing the boundary radial profile information under varying electron densities.

For all discharges reported in this paper, the plasma current is sustained as a constant, and the boundary safety factor is modified solely by adjusting the toroidal magnetic field, considering that toroidal magnetic field can affect turbulence and transport, but has no effect on the density limit.

3. Increase in edge turbulence and transport prior to the onset of HFSHD

Previous experiments have shown that the collapse of edge flow shear is a potential trigger for density limit disruption [37]. Interestingly, this collapse of the edge shear flow precedes the actual disruption considerably. In the J-TEXT, the particular behavior has been observed in the edge region as the line-averaged density approached the density limit. The temporal traces for a typical density ramping discharge are shown in figure 2. This discharge has parameters of $I_P = 120\,\mathrm{kA}$, $B_t = 1.7\,\mathrm{T}$, $q_a = 4.4$. It is notable that the density limit disruption occurs at $t = 600\,\mathrm{ms}$ and the maximum central line-average density is $\bar{n}_{e0} = 4.4 \times 10^{19}\ \mathrm{m}^{-3} = 0.75\, n_G$. The central line-averaged electron density keeps ramping up steadily during the constant plasma current ($200\,\mathrm{ms} < t < 600\,\mathrm{ms}$). Figures 2(*e*) and (*f*) present the HFS-LFS edge asymmetries in H_α emission and line-averaged electron density, signifying the emergence of a localized high-density front at $t = 0.48s$ ($\bar{n}_{e0} = 3.4 \times 10^{19}\mathrm{m}^{-3}$). Figure 2(*g*) compares the visible radiation before (0.44 s) and after (0.54 s) the arising of HFS-LFS asymmetry. The red dotted line is the estimated last closed flux surface (LCFS). It is obvious that the radiation at the HFS edge is much stronger after the emergence of HFS-LFS asymmetry, and the high-density front enters into the main plasma region. Figure 2(*h*) presents the profiles of 17-channel line-averaged densities, which manifests that the high-density front is localized at the HFS edge. All these features of the high-density front presented here are highly consistent with the phenomena of MARFE [31] or HFSHD [32] in our previous publications. However, the HFS limiter has been removed in this experiment, and there is no interaction at all between the core plasma and the machine chamber at the HFS edge. In this case, one can expect that the source location of the impurity is from a region other than the HFS edge, supposing that the impurity is mainly produced by the interaction between the plasma and the first wall. Interestingly, a localized high-density front is still observed at the HFS edge given that the impurity source is minimal at the HFS edge. This indicates that a direct, local plasma-wall interaction in the HFS is not a necessary condition for the formation of MARFE or HFSHD. This finding can be contrasted with results from TEXTOR, where the influence of local recycling was explicitly demonstrated using a Dynamic Ergodic Divertor (DED). In these experiments, creating a localized recycling source on the HFS directly triggers a MARFE, whereas homogenizing the recycling with a dynamic DED field suppressed it [47]. Therefore, we propose that the enhancement of turbulent particle transport might be the primary candidate for creating the local high-density, low-temperature conditions required for the MARFE or HFSHD to develop. Based on this thought, we will call the phenomenon of localized high-density HFSHD in the rest of this article.

Figures 3(*b*)–(*d*) display the temporal evolution of the autopower spectrum pertaining to (*b*) the floating potential, (*c*) the ion saturation current, and (*d*) the poloidal electric field, as measured by CLP. The shot in figure 3 is the same as the one presented in figure 2. Meanwhile, figure 3(*a*) presents

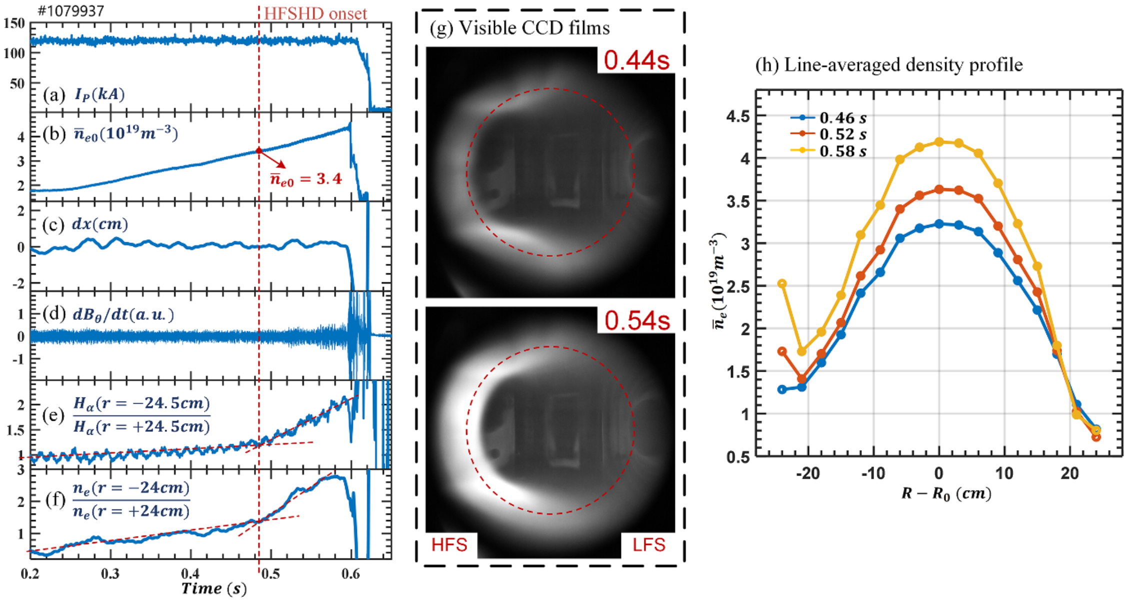

Figure 2. A typical density limit disruption discharge. (*a*) The total plasma current, (*b*) central line-averaged density measured by FIR polarimeter–interferometer, (*c*) the plasma horizontal displacement, (*d*) the edge magnetic coil signal, (*e*) the H_α emission asymmetry between the edge channel of HFS and LFS, (*f*) the density asymmetry between the edge channel of HFS and LFS measured by POLARIS, (*g*) visible CCD films before (0.44 s) and after (0.54 s) the formation of HFSHD, and (*h*) 17-channel line-averaged density profile at three time slices.

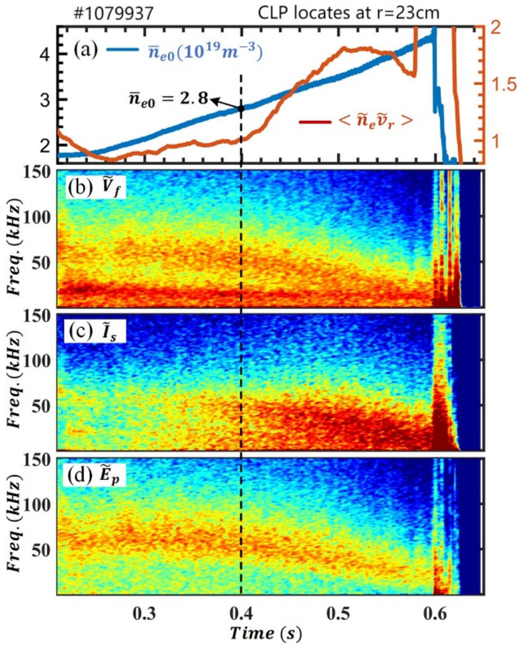

Figure 3. Corresponding to figure 2, the time evolution of (*a*) central line-averaged density (blue lines) and edge particle flux (red lines), auto-power spectrum of (*b*) floating potential, (*c*) ion saturation current, and (*d*) poloidal electric field.

the temporal evolution of the electron density and total edge particle flux, which is calculated by fluctuations of density and radial velocity.

The auto-power spectrum of the floating potential shown in figure 3(*b*) reveals two distinct branches of turbulence, each bearing different characteristic frequencies discernible before 0.4 s. In order to further explore the characteristics of these two different turbulences, figure 4 presents the coherence and phase difference between the floating potentials $\left(\widetilde{V}_f\right)$ at two separate poloidal locations. Two cases with different density are compared in figure 4. From the coherence spectrum for the low density case (figure 4(*a*)), the two turbulence branches with distinct characteristic frequencies are obvious. The low-frequency (LF) one has a characteristic frequency of $f \approx 15\,\mathrm{kHz}$ and a narrow frequency range, exhibiting a coherent mode. The high-frequency (HF) one has a characteristic frequency of $f \approx 60\,\mathrm{kHz}$ and a medium frequency range, which seems to be a quasi-coherent mode (QCM). Besides, the poloidal wavenumber of the LF coherent mode is close to zero, as indicated by the near-zero phase difference shown in figure 4(*b*). This feature is consistent with the characteristics of geodesic acoustic modes (GAMs) [39], which exhibits toroidal and poloidal symmetry with a finite radial wavenumber. Additionally, the LF coherent mode is unobserved in the auto-power spectrum of ion saturation flow and poloidal electric field, as evidenced in figures 3(*c*) and (*d*). This fact can further prove that it is GAM, which is more obvious on fluctuations of poloidal velocity and potential, rather than ion saturation current and plasma density. Moreover, the theoretical GAM frequency calculated by $f_{\mathrm{GAM}} = \sqrt{T_i + T_e/m_i}/2\pi R_0$ is around $16\,\mathrm{kHz}$ if we assume that $T_i \approx T_e \approx 35\,\mathrm{eV}$ (measured by the CLP in figures 6 and 9), which is close to the experimental observation (15kHz). Regarding the HF QCM, the phase difference between the two potentials depicted in figure 4(*b*) interestingly shows a shift from negative to positive over the peak frequency of the broadband mode. This implies that the wavelength of the mode is close to the distance between the two distributed potential probes ($d = 7\,\mathrm{mm}$). Therefore, it can

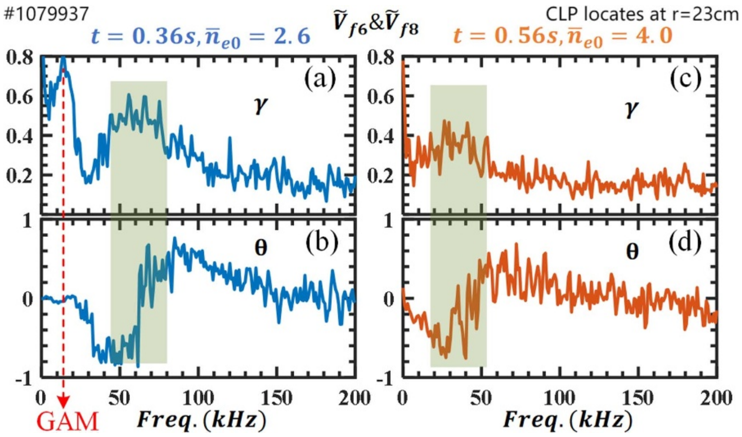

Figure 4. Corresponding to figure 3, (*a*) & (*c*) coherence and (*b*) & (*d*) phase difference between two poloidal separated floating potential $\widetilde{V}_f$, in different central line-averaged density.

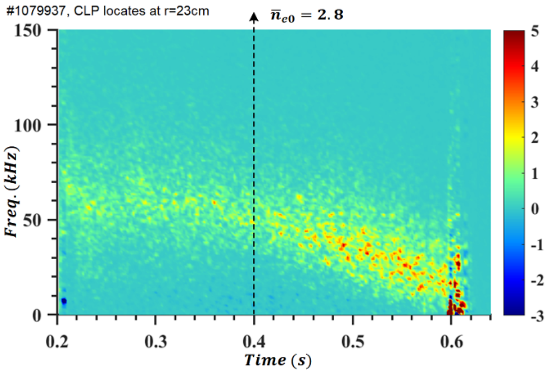

Figure 5. Corresponding to figure 3, the approximate turbulent particle flux spectral density function calculated by $\Gamma(\omega) \approx |P_{I_sE_\theta}(\omega)|\cos[\theta_{I_sE_\theta}(\omega)]/B_t = \sqrt{P_{I_s}(\omega)P_{E_\theta}(\omega)}\gamma_{I_sE_\theta}(\omega)\cos[\theta_{I_sE_\theta}(\omega)]/B_t$.

be deduced that the poloidal wave number of this broadband mode is approximately $k_\theta = 1/d \approx 1.4\,\mathrm{cm}^{-1}$.

At the time of 0.4 s, the total particle flux (red line in figure 3(*a*)) and the fluctuation of the ion saturation current (figure 3(*c*)) start to increase significantly. At the same time, the characteristic frequency of the HF QCM decreases. From 0.4 s to 0.5 s, the radial particle flux at the edge experiences a surge of 100% (figure 3(*a*), red line), while the central line-average electron density merely increases by 10% (figure 3(*a*), blue line). Moreover, figure 5 presents the approximate turbulent particle flux spectral density function, which is calculated by $\Gamma(\omega) \approx |P_{I_sE_\theta}(\omega)|\cos[\theta_{I_sE_\theta}(\omega)]/B_t = \sqrt{P_{I_s}(\omega)P_{E_\theta}(\omega)}\gamma_{I_sE_\theta}(\omega)\cos[\theta_{I_sE_\theta}(\omega)]/B_t$, where $\gamma_{I_sE_\theta}(\omega)$ and $\theta_{I_sE_\theta}(\omega)$ is the coherence and phase difference between the $\tilde{I}_s$ and $\tilde{E}_\theta$. The influence of the electron temperature T_e fluctuation is ignored in our calculation, so the density fluctuation is substituted by the fluctuation of the ion saturation current I_s. Comparing figures 5 and 3(*d*), it is obvious that the turbulent particle flux has a similar characteristic frequency to the HF QCM fluctuation. Therefore, it can be concluded that the radial particle flux is primarily contributed by the HF QCM fluctuations. In addition, the GAM fluctuation ($f \approx 15\,\mathrm{kHz}$) almost does not induce any particle transport, which is consistent with the theory. It is worth noting that the GAM fluctuation disappears in the high-density plasma as shown in figure 4(*c*). This indicates that the enhancement of I_s fluctuations and particle transport in high-density plasmas co-occur with the depression of the GAM.

Concluding the above experimental observations, after the plasma density surpasses a critical value, several concurrent phenomena are observed at the edge, including the enhancement of a QCM, the suppression of the GAM, and an increase in radial particle transport. These results suggest that the QCM fluctuations play a crucial role in boundary transport. Furthermore, we observe that its growth coincides with the suppression of the GAM and the collapse of the E_r shear, suggesting that the QCM is unleashed as these regulatory mechanisms weaken at higher density.

In order to investigate the evolution of edge profiles as the plasma density approaches the density limit, we have conducted a series of pulses (/#1079986/#1079987/#1079988) with consistent discharge parameters ($I_P = 120\mathrm{kA}, B_t = 1.7\mathrm{T}$) and incrementally increasing density shot by shot. The boundary profiles can be obtained by moving the CLP probe during the flat-top phase of density. As demonstrated in figure 6, a collapse of the sheared electric field around the LCFS ($r - a = 0$) is observed as the central line-averaged density escalates from 2 to $2.7 \times 10^{19}\mathrm{m}^{-3}$. Moreover, the edge temperature (figure 6(*b*)) around the LCFS is significantly decreased, while the electron density (figure 6(*a*)) there is not largely changed. It is worth noting that the discharge parameters of the three shots in figure 6 are identical to the shot in figures 3–5. Thus, they should share the same critical density threshold for the enhancement of turbulence and transport. By synthesizing the results from figures 3 and 6, we can infer that the collapse of the sheared radial electric field in the edge region is followed by a sudden increase in the intensity of the ion saturation current perturbation and the edge particle flux.

As illustrated in previous publications [3, 31, 48], the plasma current shrinkage induced by MARFE or HFSHD could be the direct cause of MHD instability and major disruption. The enhancement of turbulence and transport could

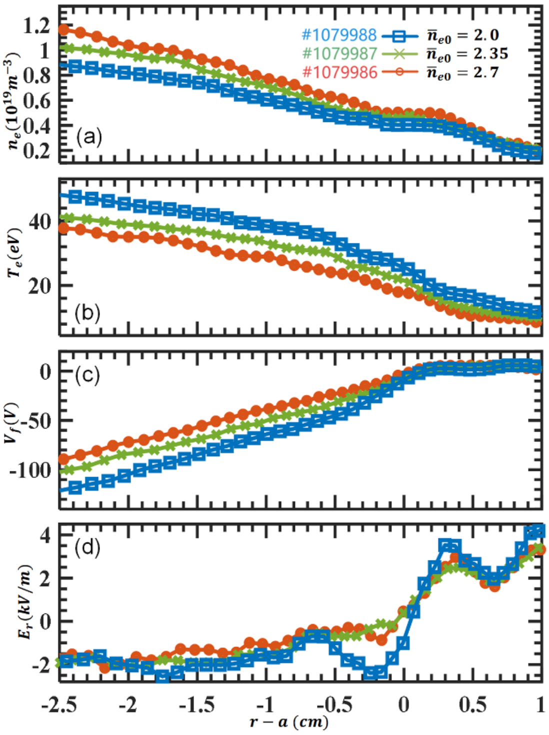

Figure 6. Profiles of (a) electron density, (b) electron temperature, (c) floating potential and (d) edge radial electric field E_r. These profiles are obtained while keeping the plasma density constant in a single shot. The blue, green and red lines represent three line-averaged densities $\bar{n}_{e0} = 2/2.35/2.7 \times 10^{19}\mathrm{m}^{-3}$ respectively.

be responsible for edge cooling and the emergence of MARFE or HFSHD. The rest of this paper will primarily explore the correlation between the turbulent transport and HFSHD. As stated in our previous publication [32], the occurrence of the HFSHD front can be identified by the ratio of the line-averaged density at the edge between HFS and LFS. As demonstrated in figure 2, when the central line-average density exceeds $\bar{n}_{e0} > 3.4 \times 10^{19}\mathrm{m}^{-3}$, the HFS line-average density increases rapidly and the asymmetry develops significantly. This indicates that a local high-density plasma region is formed at the HFS edge as the plasma density exceeds a critical value ($n_{\mathrm{crit}} = 3.4 \times 10^{19}\mathrm{m}^{-3}$ in this discharge). Such observations are representative of the characteristic features of the HFSHD front phenomenon, as described in [27, 28, 32].

To summarize the sequential phenomena as the plasma density approaches the density limit, a collapse of the sheared electric field is first observed, followed by an abrupt increase in electron density fluctuations and edge particle flux, and later on the HFSHD front appears. Based on the sequence of these events, it can be speculated that the collapse of E_r shear and subsequent increase in turbulent transport is the primary trigger for density limit disruption on tokamaks. Thermal-radiation instabilities like MARFE and HFSHD, as direct triggers for MHD and major disruption, might be a result of increased transport. It is worth noting that the physical mechanism of the MARFE or HFSHD triggering MHD has been illustrated in our previous article [31].

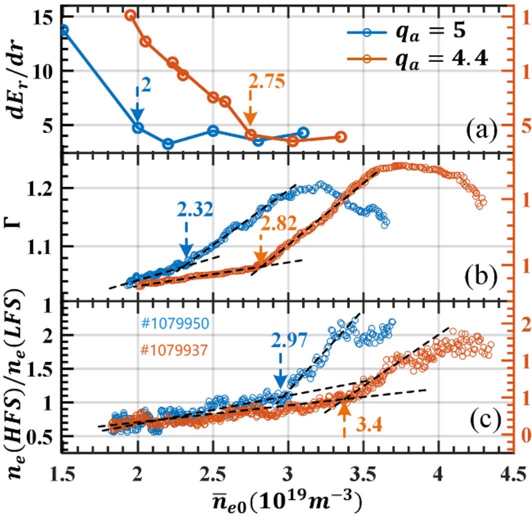

Figure 7. Traces of (a) radial electric field (E_r) shear rate, (b) edge particle flux and (c) HFS-LFS density asymmetry against line-average density for $q_a = 5$ (blue lines) and $q_a = 4.4$ (red lines).

4. Effects of edge safety factor on boundary turbulent transport and HFSHD formation

To further verify the correlation between the increase in turbulent transport and the onset of the HFSHD front, we investigated the development of boundary turbulence and HFSHD formation in plasmas with varied q_a, considering that q_a can affect turbulence and transport, but is weakly related to the density limit [3].

In figure 7, we compare the traces of radial electric field E_r shear rate around the LCFS, edge particle flux and HFS-LFS density asymmetry as a function of line-average density for the shot shown in figure 3 (where $q_a = 4.4$) and another shot with a higher q_a value of 5. The high q_a discharge has parameters: $I_P = 120$ kA, $B_t = 2, q_a = 5$. The evolution of the particle flux and HFS-LFS density asymmetry are obtained from the discharges with increasing densities in single shot (set [I]), and the E_r shear rate is acquired from the experiments by lifting densities shot by shot (set [II]).

It is noteworthy that both shots, despite the different q_a values, undergo the same sequence of events including the collapse of E_r shear, a surge in boundary particle flux, and the emergence of the HFSHD front. The key difference, as shown in figure 7(c), is that the critical line-averaged density for the onset of the HFSHD front is significantly lower in the high q_a discharge compared to the low q_a case, demonstrating a clear inverse relationship. This trend for a precursor event is strikingly similar to the q_a dependence of the final H-mode density limit reported for JET and AUG, which also shows an inverse relationship [49]. This similarity suggests that the onset of the disruptive sequence in J-TEXT may be governed by a similar underlying edge stability physics. Conversely, our result differs from observations in the FTU limiter L-mode tokamak, where the critical density of MARFE is independent of q_a [21].

The negative correlation we observe in J-TEXT, where higher q_a promotes an earlier onset of the disruptive sequence,

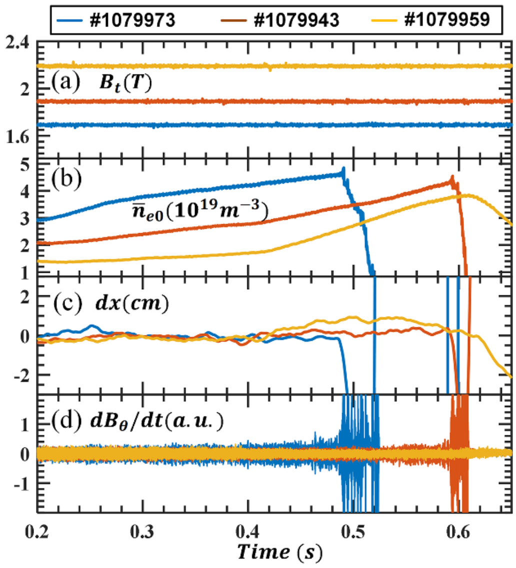

Figure 8. Time evolution of the main parameters for three typical discharges (#1079973/#1079943/#1079959) with ramping density in J-TEXT. (*a*) Toroidal field, (*b*) central line-average electron density measured by POLARIS, (*c*) horizontal plasma displacement and (*d*) the edge Mirnov coil signal.

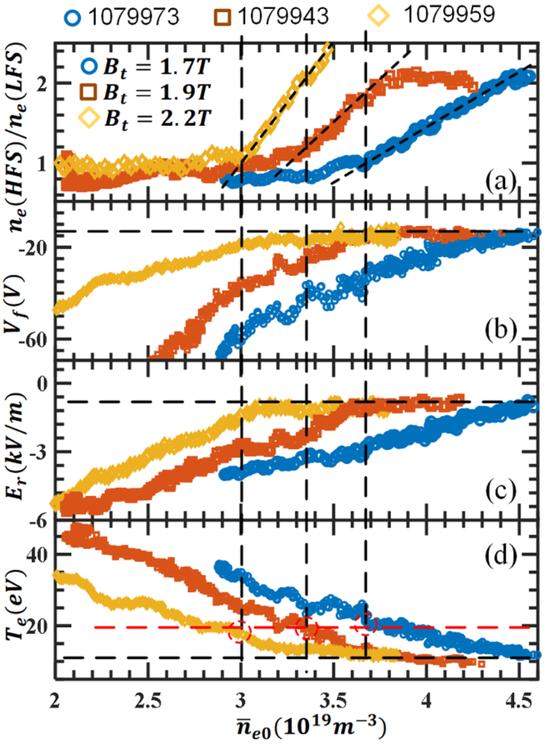

Figure 9. Traces of HFS-LFS density asymmetry measured by POLARIS (*a*) and edge parameters measured by CLP against line-average density, (*b*) floating potential (*c*) approximate $E_r \approx (V_{f,\text{step2}} - V_{f,\text{step1}})/\Delta r$, and (*d*) electron temperature for different q_a.

is, however, consistent with some MARFE studies on DIII-D [24, 50] and with the prediction by Ghendrih *et al* [51], which link higher q_a (and thus longer parallel connection lengths) to increased thermal instability at the edge. In addition, the critical densities for the collapse of E_r shear and subsequent enhancement of particle transport also demonstrate this inverse dependence on q_a, providing strong evidence that q_a is a key parameter in setting the threshold for the entire turbulence-driven sequence that initiates the density limit disruption in our plasmas.

In fact, the behaviors of turbulence and transport presented herein can elucidate why the density threshold of the HFSHD front is inversely proportional to q_a. As reported in [32], a critical value of the edge collisionality is the trigger for the onset of the HFSHD front. The enhancement of edge turbulent transport will accelerate the edge cooling and increase the edge collisionality. Therefore, in a high q_a discharge, the lower density threshold of the HFSHD front is a consequence of the lower critical density value associated with the increase in turbulent transport.

The experimental observations detailed above suggest that the edge turbulent transport plays an important role in the emergence of the HFSHD front. At the same time, the HFSHD front also impacts the evolution of boundary parameters. Discharges in the following were conducted with a constant plasma current of $I_P = 120\,\text{kA}$ and a varying toroidal field $B_t = 1.7/1.9/2.2\,\text{T}$, in order to scan the safety factor while maintaining the Greenwald density limit. Figure 8 shows the main traces for the three typical discharges (#1079973/#1079943/#1079959) with ramping density in J-TEXT. In these shots, the CLP was sustained at $r = 23\,\text{cm}$, to obtain the evolution of edge parameters along with the increasing density. The plasma density is increased by continuous gas-puffing in each shot, as shown in figure 8(*b*). Also, shots #1079973 and #1079943 disrupt at similar density, caused by the density limit. This result confirms that the density limit is weakly related to B_t or q_a. The three plasmas in figure 8 have similar positions, as indicated by horizontal displacement in figure 8(*c*). In addition, the poloidal magnetic field fluctuations measured by the Mirnov coil in figure 8(*d*) indicate that the precursor magnetic fluctuations are pretty low before the onset of $m/n = 2/1$ tearing mode (e.g. 0.49 s in #1079973 and 0.59 s in #1079943). The precursor magnetic fluctuations in higher B_t plasma is significantly lower than that in lower B_t plasma, suggesting that higher B_t or q_a can stabilize the MHD instabilities.

Corresponding to the three shots in figures 8 and 9 shows the HFS-LFS density asymmetry and key edge parameters measured by CLP at $r = 23\,\text{cm}$ against the central line-averaged density. The rapid rise in density asymmetry, shown in figure 9(*a*), is a characteristic feature of the emergence of the HFSHD front. Notably, the critical density threshold for the appearance of the HFSHD front appears to be inversely proportional to q_a, a finding consistent with our previous work [32].

Figures 9(*b*)–(*d*) present local edge parameters measured at $r = 23\,\text{cm}$. A persistent decrease in both the floating potential (V_f, figure 9(*b*)) and the electron temperature (T_e, figure 9(*d*)) is observed preceding the appearance of the HFSHD front. To provide a more direct assessment of the radial electrical field (E_r), we have calculated an approximation of E_r using the difference in the floating potential between the two radially separated steps of the CLP ($E_r \approx - \triangle V_f / \triangle r$), where $\triangle V_f = V_{f,\mathrm{step1}} - V_{f,\mathrm{step2}}$. The radial separation $\triangle r = 2.5\,\mathrm{mm}$, which is very small. Thus, the difference in electron temperature between the two steps is expected to be negligible. The E_r is shown in figure 9(c), which confirms the trend inferred from the floating potential: the E_r at the edge continuously decreases as the plasma density is ramped up. Importantly, the evolution of all these edge parameters (V_f, E_r and T_e) is strongly influenced by the edge safety factor q_a. The decrement of V_f, E_r and T_e at the edge is discernibly more premature in high q_a plasmas compared to low q_a discharges. In other words, for a given plasma density, the edge is characterized by a lower T_e and a weaker E_r in discharges with a higher q_a.

Subsequent to the emergence of the HFSHD front, both the edge V_f and T_e tend to saturate at certain values. These critical density thresholds at which saturation occurs are inversely proportional to q_a, which mirrors the behavior of the density threshold of the HFSHD front. Interestingly, the final saturation values for both the floating potential and electron temperature appear to be independent of q_a. This implies that the plasma parameters within the radial region affected by the HFSHD front are quite stable, regardless of the q_a value. As pointed out in our previous publication [32], the HFSHD front stems from the HFS SOL region, and expands radially and poloidally. A fully developed HFSHD front can extend to a radial location of $r = 20\,\mathrm{cm}$, which is significantly deeper than the location of CLP ($r = 23$ cm). As such, the CLP location is significantly impacted by the HFSHD front once the front is adequately detected by POLARIS. Moreover, according to the one-dimensional flux tube model at the plasma edge (figure 7 in [32]), the LFS end serves as the heat source of the flux tube, under the assumption that the radial heat transport is dominated by the ballooning mode turbulence. Meanwhile, the HFS end, where the cold-dense HD front resides, acts as the heat sink. Therefore, there should be a parallel heat flow from the LFS to the HFS end, ensuring the maintenance of thermal equilibrium. The CLP measures the top of the plasma, situated in the middle of the flux tube. The observed results indicate that the plasma parameters in the mid-section of the flux tube where the HFSHD front is located, are stable. This further confirms that the HFSHD front is quite stable in contrast to MARFE. Besides, as shown by figure 9(c), the electron temperature in the flux tube affected by the HFSHD front appears to stabilize around $\sim 10\,\mathrm{eV}$. This is consistent with the peak of the radiation cooling rate observed for carbon impurity, as discussed in [52].

In addition, it is worth noting that the HFSHD front consistently occurs when the edge electron temperature drops to around $\sim 20\,\mathrm{eV}$, irrespective of the specific q_a value in the discharge. This suggests that the edge temperature plays a critical role in the formation of the HFSHD front. The evolution of the edge electron temperature further corroborates the link between the edge turbulent transport and the onset of the HFSHD front. The edge temperature is mainly determined by radial transport in Ohmic plasmas, given that the heating source is centralized at the center. The fact that the drop in edge temperature is later in low q_a discharges than the high q_a ones, supports the above hypothesis that enhancement of turbulent transport plays a crucial role in creating the conditions for the HFSHD front occurrence, likely by leading to increased edge cooling and higher collisionality at the plasma edge.

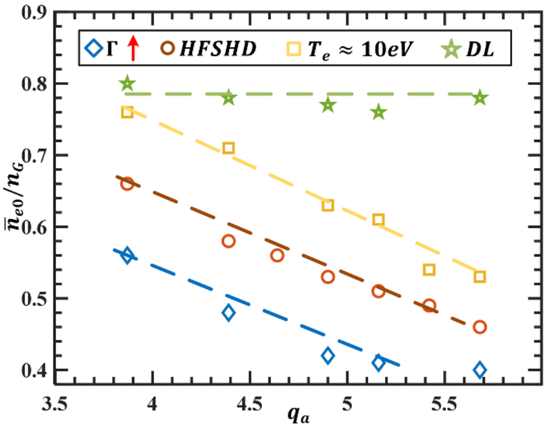

Figure 10. Statistics of density thresholds against safety factor q_a for the rapid increasing of partical flux (blue diamond), HFSHD front emergence (red circles), boundary T_e drops to 10 eV (yellow squares), and the maximum density (green pentagram).

Figure 10 shows the statistics of density thresholds for all the above physical phenomena against the boundary safety factor q_a. The series of observations documented provides valuable insights into the sequence of events that occur during plasma density ramp-ups under different q_a in tokamak experiments. The unfolding of events—from the collapse of shear flow, to the swift enhancement of boundary turbulent transport, the emergence of the HFSHD front, the saturation of boundary temperature, and ultimately, the density limit disruption—is strikingly consistent, suggesting a potentially universal mechanism underlying density limit disruption in tokamak plasmas.

Furthermore, the data show that the density thresholds for all the above physical phenomena bear an inverse relationship to q_a. This suggests that higher q_a values prompt the edge cooling and HFSHD front to manifest earlier in the plasma density ramp-up process. Nevertheless, the point of density limit disruption itself does not display a significant shift for varying q_a. This could potentially be attributed to the premature onset of edge cooling and HFSHD front, which act as catalysts for density limit disruption, while concurrently, a high q_a works to stabilize MHD instability.

5. Summary and discussion

In this paper, we report the discovery and analysis of boundary turbulence behavior and the HFSHD front as the density approaches the density limit on the J-TEXT tokamak. It is noteworthy that the HFSHD front still occurs even though the HFS limiter has been removed. This highlights that the HFSHD front is a consequence of transport, rather than being tied to impurity radiation, which is associated with plasma-wall interaction. The experiments were carried out by ohmic heating and the plasma density was increased by continuous gas puffing without the use of auxiliary systems or external drives. The following is a summary of the experimental findings:

(a) Two different branches of turbulence are observed by Langmuir probes at $\rho = 0.9a$. The LF ($f \approx 15\,\text{kHz}$) branch of turbulence is identified as GAM, characterized by its dominance in potential fluctuations, zero poloidal wavenumber ($k_\theta \approx 0$) and lack of contribution to radial particle transport. The HF ($50 \sim 80\,\text{kHz}$) QCM can be identified in the auto-power spectrum of the ion saturation flow and poloidal electric field. The edge particle flux is found to be mainly contributed by the HF QCM.

(b) After the plasma density exceeds a critical value, there is a sudden amplitude increase in HF QCM, along with a decrease in its frequency. Concurrently, the GAM is suppressed and the radial particle flux increases. In addition, a collapse of E_r shear around the LCFS is observed at a lower density than the threshold for turbulent transport enhancement. Furthermore, the appearance of the HFSHD front follows the increase in boundary turbulence.

(c) The edge floating potential and electron temperature measured by CLP consistently decrease after the increase in turbulent transport. Interestingly, they appear to stabilize at a certain value after the onset of the HFSHD front. In various q_a discharges, the HFSHD front always occurs when the edge T_e drops to around $\sim 20\,\text{eV}$, even though the density threshold is apparently different.

Our findings, which detail a sequence of events from microscale turbulence to macroscopic plasma phenomena, contribute to a more integrated understanding of the density limit disruption. The experimental evidence from J-TEXT suggests a causal chain where the enhancement of edge turbulent transport acts as the primary trigger. This enhanced transport leads to edge cooling and the subsequent formation of the HFSHD front, which further induces the shrinkage of the current density profile. This current profile contraction then creates favorable conditions for the growth of a 2/1 tearing mode, which ultimately culminates in a major disruption, as illustrated in our previous study [31]. This multi-stage, multi-scale model of the density limit pathway is consistent with a broad range of findings in the literature, which demonstrate that intervening at any point in this causal chain can effectively raise the operational density limit. For instance, Ke *et al* [40] showed that suppressing the initial step of edge turbulence using electrode biasing led to an increased density limit on J-TEXT. Similarly, Liang *et al* [47] demonstrated that using a DED on TEXTOR to suppress the MARFE formation—an intermediate step in our proposed chain—also resulted in a higher accessible density. Furthermore, Hu *et al* [53] successfully applied resonant magnetic perturbations on J-TEXT to directly suppress the final link in the chain, the 2/1 tearing mode, which again pushed the density limit upward. These collective results strongly support our view that the density limit is not a single event, but a complex sequence of interconnected physical processes. In this context, the recent, unprecedented results from the Madison Symmetric Torus (MST), when operated as a tokamak, are particularly illuminating [54]. In these experiments, stable plasmas were sustained at densities up to 10 times the Greenwald limit. This remarkable achievement was made possible by two unique engineering features: a thick, close-fitting, conductive wall that passively stabilizes MHD modes, and a powerful, feedback-controlled power supply that active maintains the plasma current and flat current profile, which is also beneficial for MHD stabilization. The MST results strongly suggest that the density limit observed in many conventional tokamaks is not an immutable law of plasma physics, but rather a consequence of a specific instability pathway that begins with transport phenomena and ends with an MHD collapse. If this final MHD consequence can be mitigated, as demonstrated in MST, the operational density space can be dramatically expanded. However, these engineering features are unique to the MST device and are not representative of conventional tokamaks.

It is worth noting that the pattern of sequential events observed in J-TEXT is consistent in various density climbing discharges. The density thresholds for these phenomena are all inversely proportional to q_a. These results further emphasize the crucial role that edge turbulent transport plays in the density limit disruption. In higher q_a discharge, the lower density threshold for edge cooling and the HFSHD front can be attributed to the earlier collapse of E_r shear and an increase in turbulent transport during the ramp-up of plasma density. Additionally, the impact of q_a on the density threshold for the collapse of E_r shear can be elucidated through the theory proposed by Hajjar *et al* [38]. According to their theory, as the plasma response passes from adiabatic ($\alpha > 1$) to hydrodynamic ($\alpha < 1$), the edge zonal shear layer collapses and turbulence is enhanced. The key variable α, the adiabaticity parameter, equals $k_z^2 v_{\text{th}}^2 / (\upsilon_{ei} |\omega|)$. Here, k_z represents the parallel wavenumber, which can be estimated to be $\sim 1/qR$. As a result, α is inversely dependent on q_a, suggesting a lower density threshold for the collapse of the edge shear layer in a higher q_a discharge.

Interestingly, the density limit itself exhibits a very weak dependence on q_a. This could potentially be interpreted as the cumulative effects of q_a on micro-turbulence and macro-MHD. On one hand, the higher the q_a could lead to a lower the density threshold for the collapse of E_r shear and resultant HFSHD front, which is detrimental to plasma confinement. On the other hand, higher q_a values tend to stabilize the MHD instability. Taken together, from a qualitative point of view, different q_a values do not significantly impact the final value of the density limit disruption. It is important to note that the above speculations are qualitative rather than quantitative. We will further conduct simulation studies in the future to demonstrate the feasibility of these speculations.

Acknowledgment

This work is supported by the National MCF Energy R&D Program under Grant No. 2018YFE0310300 and the National Natural Science Foundation of China under Grant Nos. 11905080 and 51821005. This work has been also part-funded by the EPSRC Energy Programme [Grant No. EP/W006839/1].

ORCID iDs

Peng Shi 0000-0002-1853-0726
Li Gao 0000-0001-5758-3516
Hongjuan Sun 0000-0003-0880-0013
Chengshuo Shen 0000-0003-3503-8140
Yanqiu Chen 0009-0003-0762-0448
Zhipeng Chen 0000-0002-8330-0070
Lu Wang 0000-0002-5881-6139
Zhongyong Chen 0000-0002-8934-0364
Nengchao Wang 0000-0001-6797-2398
Zhoujun Yang 0000-0002-9141-7869
Jingchun Li 0000-0001-9918-8880

References

[1] Shimada M. *et al* 2007 *Nucl. Fusion* **47** S1–S17
[2] Wan Y. *et al* 2017 *Nucl. Fusion* **57** 102009
[3] Greenwald M., Terry J.L., Wolfe S.M., Ejima S., Bell M.G., Kaye S.M. and Neilson G.H. 1988 *Nucl. Fusion* **28** 2199–207
[4] Allen J.M. *et al* 1986 *Plasma Phys. Control. Fusion* **28** 101–12
[5] Stabler A. *et al* 1992 *Nucl. Fusion* **32** 1557
[6] Schuller F.C. 1995 *Plasma Phys. Control. Fusion* **37** A135
[7] Fielding S.J., Hugill J., McCracken G.M., Paul J.W.M., Prentice R. and Stott P.E. 1977 *Nucl. Fusion* **17** 1382–5
[8] Zanca P., Sattin F. and Escande D.F. 2019 *Nucl. Fusion* **59** 126011
[9] Stacey W.M. and Petrie T.W. 2000 *Phys. Plasmas* **7** 4931–41
[10] Waidmann G. and Kuang G. 1992 *Nucl. Fusion* **32** 645–54
[11] Stacey W.M. 2001 *Phys. Plasmas* **8** 3673–88
[12] Greenwald M. 2002 *Plasma Phys. Control. Fusion* **44** R27
[13] Maingi R., Mahdavi M.A., Petrie T.W., Baylor L.R., Jernigan T.C., La Haye R.J., Hyatt A.W., Wade M.R., Watkins J.G. and Whyte D.G. 1999 *J. Nucl. Mater.* **266–9** 598–603
[14] Maingi R. and Mahdavi M.A. 2005 *Fusion Sci. Technol.* **48** 1117–26
[15] Lipschultz B., LaBombard B., Marmar E.S., Pickrell M.M., Terry J.L., Watterson R. and Wolfe S.M. 1984 *Nucl. Fusion* **24** 977–88
[16] Lipschultz B., Terry J.L., Boswell C., Hubbard A., LaBombard B. and Pappas D.A. 1998 *Phys. Rev. Lett.* **81** 1007–10
[17] Boody F.P., Bush C.E., Medley S.S., Park H.K. and Schivell J.F. 1987 *J. Nucl. Mater.* **145–7** 196–200
[18] Sergienko G., Pospieszczyk A., Lehnen M., Brix M., Rapp J., Schweer B. and Greenland P.T. 2001 *J. Nucl. Mater.* **290–293** 720–4
[19] Nishitani T., Ishida S., Hosogane N., Sugie T., Itami K. and Takeuchi H. 1990 *J. Nucl. Mater.* **176–7** 763–8
[20] Gao X. *et al* 2000 *J. Nucl. Mater.* **279** 330–4
[21] Pucella G. *et al* 2013 *Nucl. Fusion* **53** 083002
[22] Mertens V. *et al* 1994 *Plasma Phys. Control. Fusion* **36** 1307–25
[23] Loarte A. *et al* 1998 *Nucl. Fusion* **38** 331–71
[24] Petrie T.W., Kellman A.G. and Mahdavi M.A. 1993 *Nucl. Fusion* **33** 929–54
[25] Potzel S. *et al* 2015 *J. Nucl. Mater.* **463** 541–5
[26] Potzel S., Wischmeier M., Bernert M., Dux R., Müller H.W. and Scarabosio A. 2013 *Nucl. Fusion* **54** 13001–19
[27] Manz P., Potzel S., Reimold F. and Wischmeier M. (ASDEX Upgrade Team) 2017 *Nucl. Mater. Energy* **12** 1152–6
[28] Reimold F., Wischmeier M., Potzel S., Guimarais L., Reiter D., Bernert M., Dunne M. and Lunt T. 2017 *Nucl. Mater. Energy* **12** 193–9
[29] Kelly F., Maingi R., Maqueda R., Menard J. and Paul S. 2009 *J. Nucl. Mater.* **390–391** 436–9
[30] Zeng L., Tudisco O., Gao W., Zhang S., Gao X., Pucella G. and Apruzzese G. 2013 *J. Nucl. Mater.* **438** S917–S920
[31] Shi P. *et al* 2017 *Nucl. Fusion* **57** 116052
[32] Shi P., Sun H., Zhuang G., Cheng Z., Gao L., Chen Z., Li J., Zhou Y. and Zhou C. 2021 *Plasma Phys. Control. Fusion* **63** 125010
[33] Brower D.L. *et al* 1991 *Phys. Rev. Lett.* **67** 200–3
[34] LaBombard B., Boivin R.L., Greenwald M., Hughes J., Lipschultz B., Mossessian D., Pitcher C.S., Terry J.L. and Zweben S.J. 2001 *Phys. Plasmas* **8** 2107
[35] D’Ippolite D.A. and Myra J.R. 2006 *Phys. Plasmas* **13** 062503
[36] Hong R., Tynan G.R., Diamond P.H., Nie L., Guo D., Long T., Ke R., Wu Y., Yuan B. and Xu M. 2018 *Nucl. Fusion* **58** 016041
[37] Long T. *et al* 2021 *Nucl. Fusion* **61** 126066
[38] Hajjar R.J., Diamond P.H. and Malkov M.A. 2018 *Phys. Plasmas* **25** 062306
[39] Sun Y., Chen Z.P., Zhu T.Z., Yu Q., Zhuang G., Nan J.Y., Ke X. and Liu H. 2014 *Plasma Phys. Control. Fusion* **56** 015001
[40] Ke R. *et al* 2022 *Nucl. Fusion* **62** 76014
[41] Tokar M.Z. 2003 *Phys. Rev. Lett.* **91** 095001
[42] Zhuang G. *et al* 2011 *Nucl. Fusion* **51** 094020–11
[43] Wang N.C. *et al* 2022 *Nucl. Fusion* **62** 042016
[44] Wang Y.H. *et al* 2022 *Plasma Sci. Technol.* **24** 064001
[45] Zhang X.L., Cheng Z.F., Hou S.Y., Zhuang G. and Luo J. 2014 *Rev. Sci. Instrum.* **85** 11E420
[46] Yang Q. *et al* 2022 *Plasma Sci. Technol.* **24** 54005
[47] Liang Y. *et al* 2005 *Phys. Rev. Lett.* **94** 105003
[48] Li X. *et al* 2023 *AIP Adv.* **13** 035037
[49] Huber A. *et al* 2017 *Nucl. Mater. Energy* **12** 100–10
[50] Maingi R. *et al* 1997 *Phys. Plasmas* **4** 1752–60
[51] Ghendrih P.H., Petrie T.W., Lasnier C., Leonard A.W. and Maingi R. 1995 *J. Nucl. Mater.* **220–222** 305–9
[52] Neuhauser J., Schneider W. and Wunderlich R. 1986 *Nucl. Fusion* **26** 1679
[53] Hu Q., Wang N., Yu Q., Ding Y., Rao B., Chen Z. and Jin H. 2015 *Plasma Phys. Control. Fusion* **58** 025001
[54] Hurst N.C., Chapman B., Sarff J., Almagri A., McCollam K., Den Hartog D., Flahavan J. and Forest C. 2024 *Phys. Rev. Lett.* **133** 055101